Proceedings of the 9ICEG
9th International Congress on Environmental Geotechnics
25-28 June, 2023 | Chania, Greece

https://doi.org/10.53243/ICEG2023-138

A multi-objective optimization approach for identifying the key influencing factors in hydrate gas production

X. Feng[1], M. L. Zhou[2], L. Tan[3], and F. Liu*[4]

[1]*Doctoral student, Department of Geotechnical Engineering, Tongji University, Shanghai, China, email: fengxin_@tongji.edu.cn*

[2]*Associate Professor, Department of Geotechnical Engineering, Tongji University, Shanghai, China, email: zhoum@tongji.edu.cn*

[3]*Postdoctor, Department of Geotechnical Engineering, Tongji University, Shanghai, China, email: tanlin@tongji.edu.cn*

[4]*Professor, Department of Geotechnical Engineering, Tongji University, Shanghai, China, email: liufang@tongji.edu.cn*

ABSTRACT

Production trials have shown that gas production from oceanic hydrates is not satisfactory due to problems such as low efficiency and sand production. Moreover, hydrate exploitation could pose a risk to the marine environment by causing catastrophic seafloor instability. Thus, it is of utmost importance to choose an optimal site that enables economic and safe production. This paper aims at a multi-objective optimization approach to evaluate the producibility of hydrate reservoirs and identify the key influencing factors. The multi-phase coupling module Tough + Hydrate code and limit equilibrium method were adopted to populate a set of hypothetical scenarios of gas production from hydrate reservoirs by varying geological conditions and production parameters. The numerical scenarios were used to formulate indicators that characterize the producibility of a reservoir with two evaluation indexes, namely high production and low environmental impact. Sensitivity and correlation analysis within the numerical scenarios were conducted to identify the significant parameters that control the producibility indicators. The results show that there is a difference in the importance ranking of the influencing factors for the reservoir producibility. In certain combinations of production scenario parameters, the economic and safety indexes do not perturb each other. That is, single-objective optimization can be performed under these geological conditions. For perturbed combinations, the multi-objective optimization will select different preferred geological or production conditions due to the different bias of dominant objectives. The proposed approach is potentially useful for fast screening of optimal sites for extracting gas from oceanic hydrate reservoirs.

Keywords: oceanic hydrate, site selection, production response, parametric study, decision-making

1 INTRODUCTION

Natural gas hydrates are polycrystalline, non-stoichiometric, and clathrate-structured solids, which consist of natural gas molecules (primarily methane) trapped in lattices of water molecules (Sloan & Koh, 2008). As an alternative energy resource, natural gas hydrates could replace coal, petroleum and conventional natural gas in the 21st century, and thus is considered to have profound impact on the global pattern of energy supply and demand (Collett, 2002). A number of countries are actively involved in research and field-scale production trials intended for enabling commercial production (Chen & Merey, 2021). To identify optimal sites for production is the key step towards commercially viable production.

Different from exploitation of consolidated reservoirs, extracting gas from hydrates hosted in oceanic sediments causes extreme reduction in the strength of the sediments, and could prime or trigger massive submarine landslides (Hyodo et al., 2015; Zander et al., 2018). Thus, a hydrate reservoir is considered ideally producible not only because of its potential to reach a high gain but also its low environmental impact caused by production. In other words, optimizing site selection for hydrate exploitation is a multi-criteria decision-making process, in which to maximize the economic gain and to minimize the possibility of induced geohazards should be simultaneously taken into consideration.

Indexes have been proposed to measure the economic gain of hydrate exploitation, such as the cumulative gas output, and gas to water ratio during production. They can be quantified with the techniques of thermo-hydro-chemical (THC) coupled numerical simulations, which are capable to model dissociation/formation of hydrates in porous medians undergoing multi-phase fluid and heat flow. These numerical tools are further combined with mechanical analysis methods for obtaining the mechanical response of hydrate reservoirs being depleted. For instance, they are implemented into the limit equilibrium analysis of slope stability (Sultan et al., 2004; Nixon & Grozic, 2007; Tan et al., 2021) , the finite element method, or finite different method (Kong et al., 2018; Lu, Zhang, & Lu, 2017; B. Song et al., 2019) for assessing the possibility of production-induced submarine landslides. These studies prepared powerful tools for quantifying metrics required in site selection, of which however the multi-criterion decision procedure has not been fully explored.

This paper is intended to framework a multi-criteria decision making for selecting the optimal sites to produce gas from oceanic hydrate reservoirs. In this preliminary study, the cumulative gas volume over 10-year production and the onset time of slope failure under the hypothetical perturbation are chosen as the metrics of the economic gain and the environmental impact, respectively, although the proposed methodology can be applied to other sets of metrics. The influencing factors are identified by parametric studies according to the site conditions of Shenhu area in the South China Sea, where abundant hydrate resources are resided and production trials were conducted in 2017 and 2020.

2 METHODOLOGY

Figure 1 illustrates a three-step workflow for identifying the key influencing factors of the two selected metrics. The first step is to establish a simple but representative numerical model on the basis of geological and geotechnical data from the Shenhu area in the South China Sea. The central composite design (CCD) was then employed to populate a set of simulation scenarios. In the second step, the anthropological exploitation of marine hydrates (depressurization with a horizontal well) and natural seafloor warming were selected as the hypothetical triggers of hydrate dissociation to assess the economic gain and the environmental impact, respectively. The final step of slope stability was analysed within the limit equilibrium method based on an infinite slope considering the transient pore pressure and the reduced shear strength in the slope undergoing hydrate dissociation.

The coupled Thermo-Hydro-Chemical (THC) simulator is incorporated into the framework of the limit equilibrium method of slope stability analysis. The time-dependent shear strength and pore pressure in the host sediments during hydrate dissociation are computed in the THC coupled simulator and then used in the slope stability analysis to achieve a time-dependent safety factor of slope stability. The potential sliding surface in the slope is assumed to be parallel to the dip direction. The safety factor of the slope is time-dependent and calculated as equation (1). Based on the evolving factor, the onset time of slope failure is traced and utilized to assess the possibility of submarine landslides under the hypothetical perturbation. This framework is articulated in our previous work (Liu et al., 2020; Tan & Liu, 2020).

$$F_s(t) = \frac{\tau_f(t)}{\tau_d(t)} = \frac{c'(t) + \left[\sigma'_0 - u_e(t)\right]\tan\varphi'(t)}{\gamma' H(t)\sin\beta\cos\beta} \tag{1}$$

where t represents time; $\tau_d(t)$ and $\tau_f(t)$ are the shear stress and the shear strength on the failure plane located at depth H; β is the slope angle; γ' is the buoyant unit weight of the sediments; σ'_0 is the initial effective overburden stress on the failure plane; u_e is the transient excess pore pressure; and c', γ' are the effective cohesion and internal friction angle of the sediments, respectively.

The transient excess pore pressure u_e is calculated by subtracting the hydrostatic pressure u_s from the total pore pressure u that derives from the weighted gas and aqueous pore pressure according to Bishop's principle of multi-phase flow:

$$u_e(t) = u(t) - u_s = \frac{S_G(t)}{S_G(t) + S_A(t)} u_G(t) + \frac{S_A(t)}{S_G(t) + S_A} u_A(t) - u_s \tag{2}$$

where S_G and S_A are the void saturation of gas and liquid in the pore space, respectively; u_G and u_A are the pore gas pressure and the pore aqueous pressure, respectively.

The strength of the host sediment also varies over time during hydrate dissociation. Experimental studies suggest an insignificant variation in the internal friction angle of host sediments undergoing hydrate dissociation, while an apparent reduction in the cohesion (Y. Song et al., 2014). Accordingly, the internal friction angle is assumed unchanged in this study and the effective cohesion is linearly related to the hydrate saturation:

$$c'(t) = c'_0 \frac{S_H(t)}{S_{H0}} \tag{3}$$

where c'_0 is the initial effective cohesion, and S_H and S_{H0} are the transient and initial hydrate saturation, respectively.

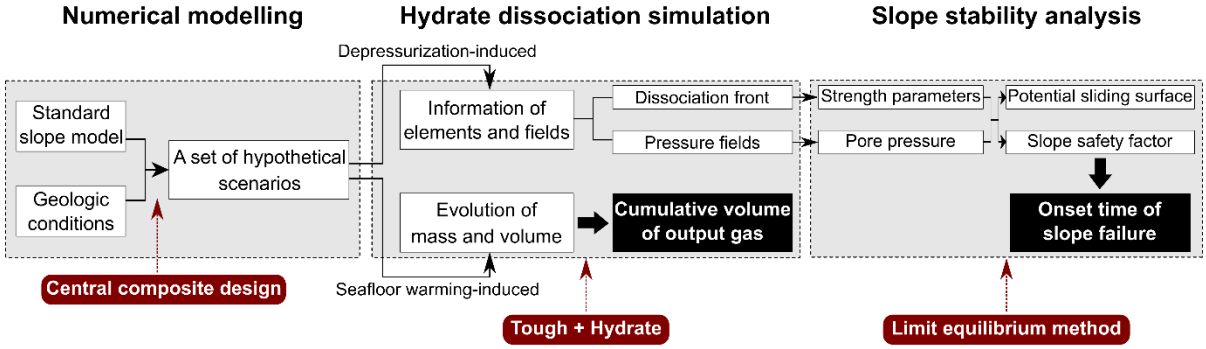

Figure 1. *A workflow for calculating two selected metrics*

2.1 Numerical model

The Tough + Hydrate code developed by the Lawrence Berkeley National Laboratory and its parallel version thereof (Moridis, 2014) were employed to simulate the hydrate gas production. The code can fully describe the non-isothermal hydrate dissociation, gas release, phase behaviour, and fluid/heat flow under conditions typical of naturally occurring methane hydrate reservoirs in complex geological media.

As shown in Figure 2, a two-dimensional slope model was constructed for a synthetic hydrate gas production site in this study. The slope model is 2000 m wide, of which the slope section is 1000 m in width. The model comprises vertically a permeable upper boundary (overburden layer, OL), a hydrate-bearing-layer (HBL) with methane hydrates, and a permeable lower boundary (underburden layer, UL). The model assumes that the HBL, with a thickness of H_2, is located at a water depth D and is overlain by a soil layer with a thickness of H_1, while the thickness of the UL is set at 40 m, which is sufficient for the fluid and heat flow through the boundaries. A horizontal well is arranged in the middle of the HBL, whose well axis is perpendicular to the slope cross section with a burial depth of h and a radius of r at the wellhead.

To attenuate the effect of domain discretization on the simulation results, the HBL allows a fine discretization with main subdivisions of Δz = 0.5 m near the production well and Δz = 1.0 m and 5.0 m towards the overburden and underburden layers. The upper and lower boundaries are subdivided into a uniform mesh grid of Δz = 20 m along the z-direction, and the uppermost and lowermost grids are regarded as fixed-state (no fluid or heat exchange) with a thickness of 0.1 m. The most essential step in the simulation is to determine the initial conditions of the hydrate reservoirs which include the distributions of pressure, temperature and hydrate saturation. The initial hydrate saturation in the HBL is set to a certain value S_h, and the OL and UL are both water-saturated layers with no hydrate or free gas. Since the methane hydrate reservoir in this area is permeable, it is assumed that the hydrostatic distribution in the system and the initial pressure can be calculated by the empirical equation (4). Once the geometry of the hydrate reservoir is determined, the initial temperature distribution in the reservoir is determined by the seafloor temperature and the geothermal gradient assuming a uniform 45 ℃/km

in the system, as given in equation (5). The spatial distribution of temperature and pressure at the end of 10 years was plotted for a case with D = 1100 m, as shown in Figures 3a and 3b.

$$P = P_{atm} + \rho_w g\ (D + Z) \tag{4}$$

where P_{atm} is the atmospheric pressure, 1.03×10^5 Pa; ρ_w is the average seawater density, 1.03 kg/m^3; g is the acceleration of gravity, 10 m/s^2; D is the water depth; and Z is the depth from the seafloor.

$$T = T_{sf} + 0.045 \times Z \tag{5}$$

where the temperature of the sea floor $T_{sf} = 373.41 \times D^{-0.6269}$ (Wang, Yan, & Song, 2006).

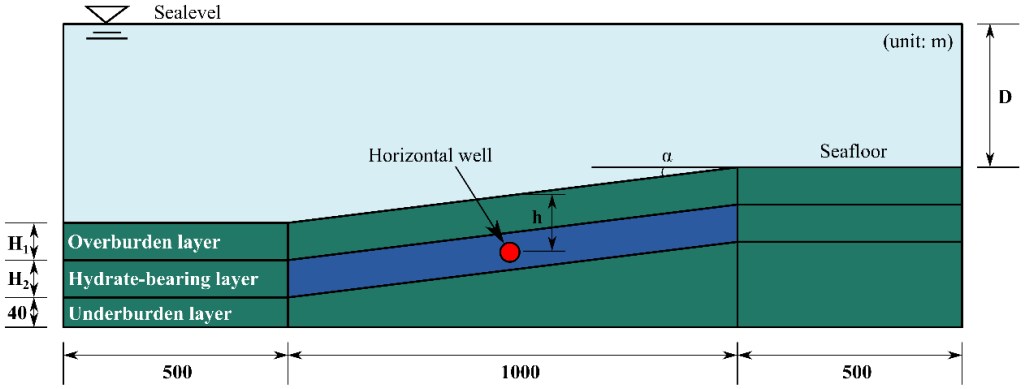

Figure 2. *Schematic of hydrate-bearing slope model*

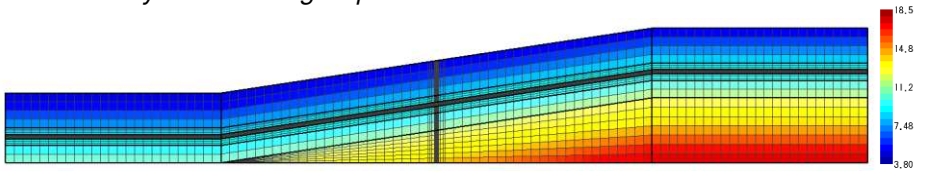

a. *Initial temperature (℃)*

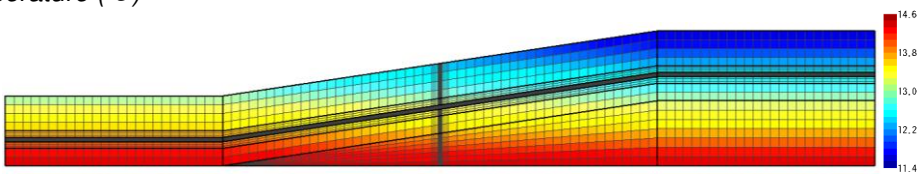

b. *Initial pressure (MPa)*

Figure 3. *Initial conditions in the reservoir of a typical scenario*

2.2 Synthetic simulation scenarios

For multiple physical processes, a full factorial experimental design is often used to analyse the relationship between the evaluation metrics and the influential factors, and even the relative contributions of the factors as well. A full factorial design refers to a design of experiments that are made up of all the factor combinations possible, in which all the levels of all the factors are coded. In this study, the cumulative gas volume over 10-year production and the onset time of slope failure are considered to be affected by eight geological factors, namely the angle of slope, the depth of water, the depth of hydrate burial, the thickness of the HBL, the hydrate saturation, the formation porosity, and the intrinsic permeability of the HBL and OL. Each factor is assigned with five quantitative values, referred to as levels of the specified factor in Table 1. The specific values for the extreme levels were determined by summarizing the maximum and minimum data range obtained from exploration in the South China Sea. Iterating through all the levels of all the factors, a total of 390,625 (5^8) experimental combinations are required. This requires a significant amount of simulation time and effort, so an optimized experimental design is desirable to generate smaller but representative trials (Goren, Recepoğlu, & Khataee, 2022).

The central composite design constitutes a full, factorial or fractional design. The points in the centre of the experimental domain and the “star” points outside this domain make it possible to estimate the

curvature of the response surface (Box & Wilson, 1951). Figure 4 illustrates the generation of the CCD. The levels of the points in a factorial design are ±1 and those in a "star" design are ±λ where $\lambda = (N)^{1/4}$. The number of trials to be performed in the CCD is determined by the following formula: $N = 2^m + 2m + N_0$ (m is the number of factors). For $m = 8$ in this study, then the $2^8 = 256$ factorial trials, 2*8 = 16 axial trials, and 1 centre trial were simulated. Table 2 below summarizes these designs.

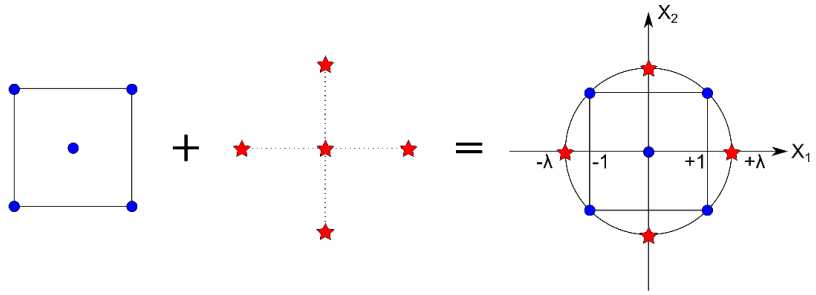

Figure 4. *Generation of a central composite design*

Table 1. *The levels of eight influential factors*

Factors	Negative extreme level	Negative factorial level	Central level	Positive factorial level	Positive extreme level
Water depth D	817 m	1000 m	1100 m	1200 m	1383 m
Burial depth H_1	23 m	60 m	80 m	100 m	137 m
Thickness of hydrate-bearing-layer H_2	12 m	30 m	40 m	50 m	68 m
Slope angle α	4°	7°	8.5°	10°	13°
Hydrate Saturation S_h	20%	26%	30%	34%	40%
Formation porosity ρ	0.30	0.36	0.40	0.44	0.50
Permeability of hydrate-bearing-layer k_1	7.5 mD	19.6 mD	26.3 mD	32.9 mD	45 mD
Permeability of overburden-layer k_2	2.6 mD	4.2 mD	5.0 mD	5.9 mD	7.5 mD

Table 2. *Experimental program*

Type	No.	D (m)	H_1 (m)	H_2 (m)	α (°)	S_h (%)	ρ	k_1 (mD)	k_2 (mD)
Factorial trials	1	1000	60	30	7	26%	0.36	19.6	4.2
	2	1000	60	30	7	26%	0.36	19.6	5.9
	...								
	255	1200	100	50	10	34%	0.44	32.9	4.2
	256	1200	100	50	10	34%	0.44	32.9	5.9
Centre trial	257	1100	80	40	8.5	30%	0.40	26.3	5.0
Star trials	258	817	80	40	8.5	30%	0.40	26.3	5.0
	259	1383	80	40	8.5	30%	0.40	26.3	5.0
	260	1100	23	40	8.5	30%	0.40	26.3	5.0
	261	1100	137	40	8.5	30%	0.40	26.3	5.0
	262	1100	80	12	8.5	30%	0.40	26.3	5.0
	263	1100	80	68	8.5	30%	0.40	26.3	5.0
	264	1100	80	40	4	30%	0.40	26.3	5.0
	265	1100	80	40	13	30%	0.40	26.3	5.0
	266	1100	80	40	8.5	20%	0.40	26.3	5.0
	267	1100	80	40	8.5	40%	0.40	26.3	5.0
	268	1100	80	40	8.5	30%	0.30	26.3	5.0
	269	1100	80	40	8.5	30%	0.50	26.3	5.0
	270	1100	80	40	8.5	30%	0.40	7.5	5.0
	271	1100	80	40	8.5	30%	0.40	45	5.0
	272	1100	80	40	8.5	30%	0.40	26.3	2.6
	273	1100	80	40	8.5	30%	0.40	26.3	7.5

3 RESULTS AND DISCUSSIONS

3.1 A typical scenario

Figures 5a, 5b, and 5c show the spatial distribution of the physical properties in the reservoir including the hydrate saturation, the temperature, and pressure in the reservoir over time in a typical scenario among the 273 representative cases (Case No, 257). As shown in Figure 5a, the low-pressure area appeared around the production well as a result of the constant pressure depressurization extraction method. Since the HBL and OL layers have higher intrinsic permeability, the low-pressure mainly expanded in these two layers, thus promoting hydrate dissociation and allowing free gas to escape to the wellhead. In Figure 3b, owing to the endothermic nature of hydrate dissociation, the sensible heat of the sediment in the vicinity of the production well was heavily depleted, and the colder pore water from the OL and UL layers (both permeable burdens) was drawn into the HBL layer by the pressure difference to compensate for the heat consumption in the HBL. However, the compensation was not very effective, and the temperature in the HBL decreased significantly, following which some secondary hydrates gradually formed on the hydrate dissociation front in the upper part of the HBL (very tiny red blob near the well in Figure 5c).

Figure 6a illustrates the evolution of the volumetric rate of hydrate-originating gas release in the accumulation (Q_R) and the cumulative volume of gas released from hydrate dissociation (V_R) over 10 years of the typical scenario No.257. The Q_R started from a high level of almost 0.005 m^3/s at the early stage, due to the large pressure difference existing between the production well and the reservoir, which promoted the release of gas from hydrate dissociation. Subsequently, the depressurization effect in the reservoir was greatly weakened as free gas and water flowed towards the well, resulting in a sudden drop in Q_R to less than 0.0002 m^3/s. During the entire production period, a cumulative volume of approximately 9.11×10^4 m^3 was obtained with an average gas production rate of 24.96 m^3/d. A higher cumulative output gas volume is considered to represent a higher economic gain, which was selected as one of the evaluation metrics.

Figure 6b displays the change in the safety factor of slope stability over time with the onset time of slope failure marked out as the typical scenario No.257. The initial slope stability is controlled by the slope angle, so the gentle slope (α = 8.5°) is stable with a safety factor greater than 3.0. The dissociation induced by seafloor warming causes a loss of soil cohesion. This phenomenon is linked to the change in hydrate saturation (Kajiyama et al., 2017). Meanwhile, the released gas expands in the confined pore space, leading to a buildup of excess pore pressure. As a result, the slope safety factor decreases with the cohesion loss and pressure build-up. Over time, the slope starts to slide when the safety factor falls below 1.0. The onset time of slope failure is determined accordingly, as another evaluation metric. And the longer the onset time, the lower the environmental impact. In the No.257 scenario, the onset time of slope failure is year 67.

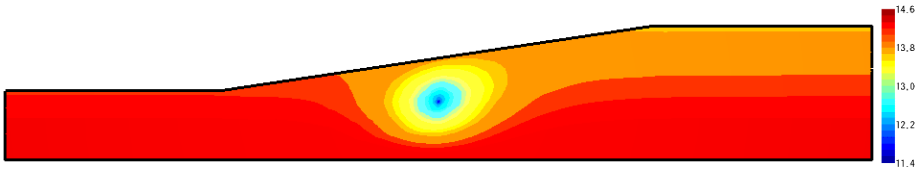

a. *Spatial distribution of the pressure at the end of 10 years (MPa)*

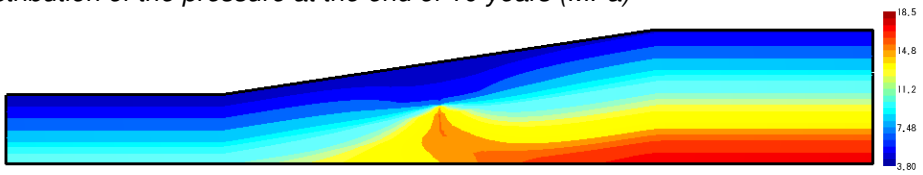

b. *Spatial distribution of the temperature at the end of 10 years (℃)*

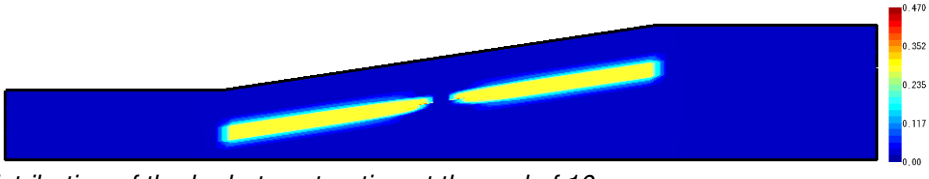

c. *Spatial distribution of the hydrate saturation at the end of 10 years*

Figure 5. *Distribution characteristics of the properties in the reservoir of the typical scenario No.257*

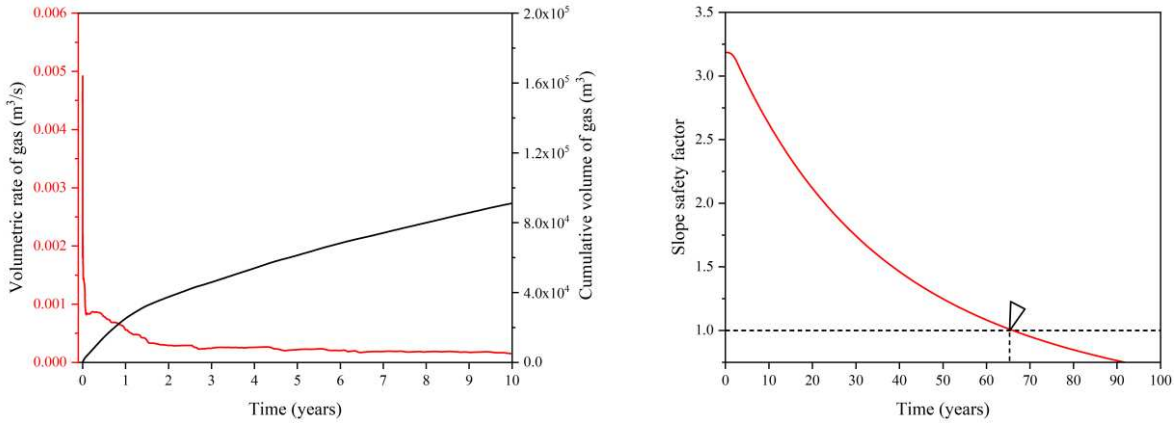

a. *The evolution of the volumetric rate and the cumulative volume of gas* ***b.*** *The evolution of the slope safety factor*

Figure 6. *Two evaluation metrics occurring in the typical scenario No.257*

3.2 Effects of the influential geological factors

The values of the cumulative gas volume and the onset time of slope failure for the corresponding 273 simulation scenarios were obtained from numerical studies. Scatter plots of the relationships between the various geological factors and the evaluation metrics were drawn as shown in Figures 7a and 7b below. A range analysis was carried out to identify and rank the geological factors influencing the economic gain and the environmental impact. For a specific factor, the average result of each level was calculated, and the range is the difference between the maximum and minimum of the five levels. The range was then divided by the mean of the trial results of all levels to obtain the dimensionless-range. As presented in Figures 8a and 8b, the importance of the eight factors can be arranged in order according to the dimensionless-range of values. For the economic gain, characterized by the cumulative gas volume, the order of significance levels of the geological factors is as follows: $H_2 > k_1 > H_1 > \alpha > D > \rho > S_h > k_2$; the order of significance levels of the geological factors influencing the environmental impact characterized by the landslide onset time is: $H_1 > \alpha > H_2 > S_h > D > \rho > k_1 > k_2$.

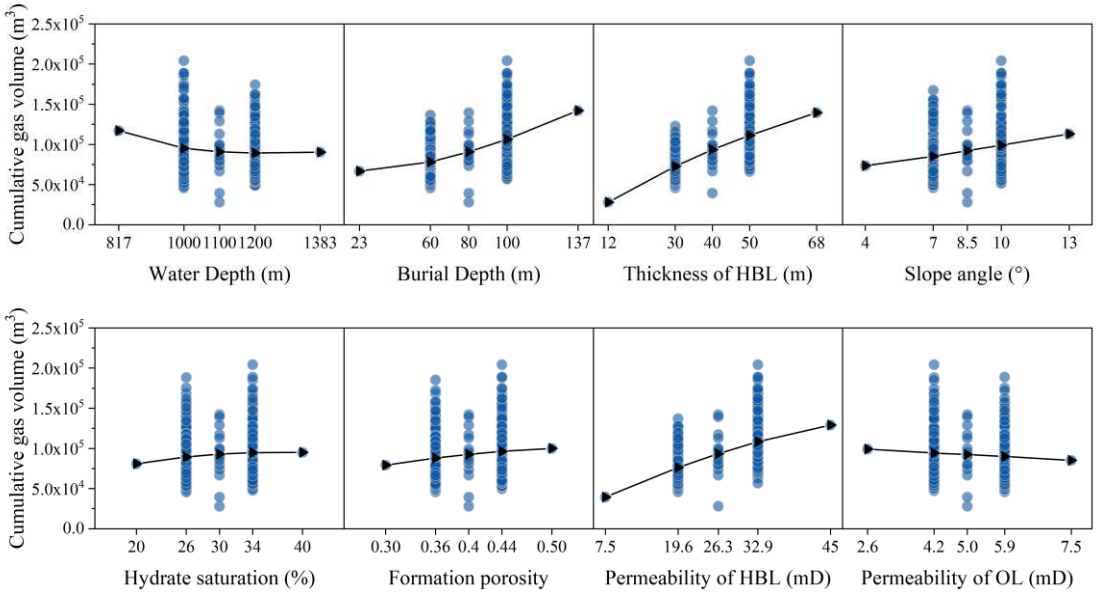

a. *Cumulative gas volume over 10 years*

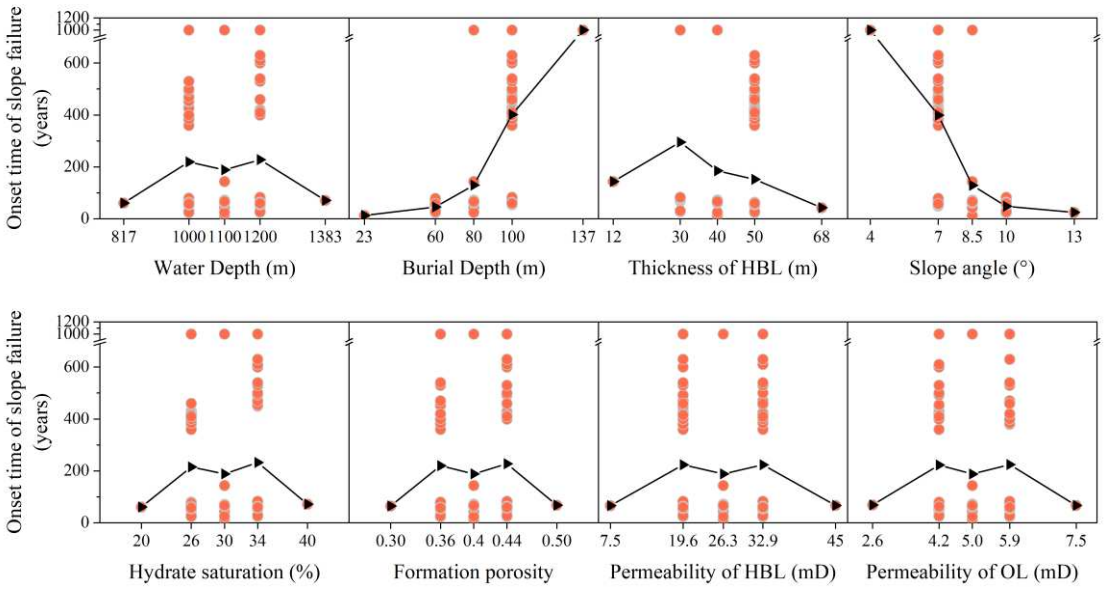

b. *Onset time of slope failure*

Figure 7. *The relationship between the geological factors and evaluation metrics*

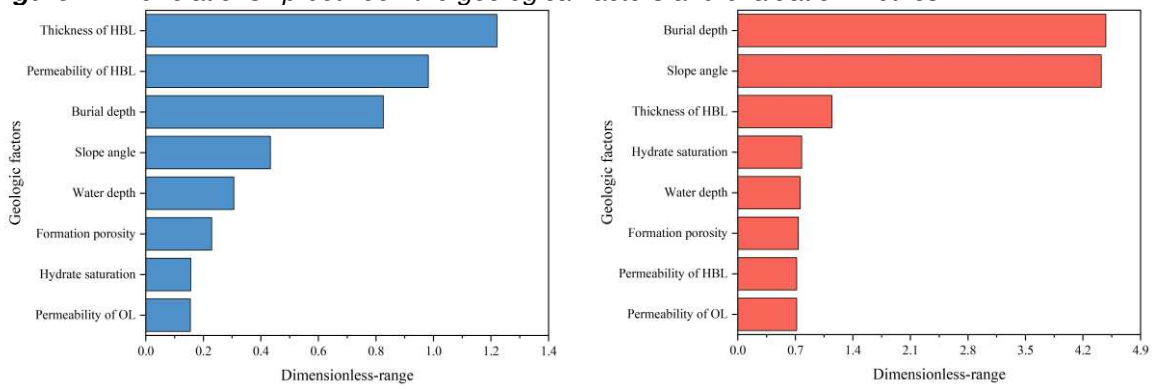

a. *Impact on the economic gain* ***b.*** *Impact on the environmental impact*

Figure 8. *Ranking of the geological factors influencing the economic and safety metrics*

3.3 Multi-objective in the production target selection

In the context of an attractive target for hydrate gas production, the economic gain should be satisfied with a high cumulative gas volume, while the environmental impact should be satisfied with a long landslide onset time. In the decision-making process for the optimal sites, the weights of the evaluation metrics also change as preferences for economic and safe production vary. The issue of weighting is not discussed in this work. A multi-objective optimization approach is proposed primarily to access the candidate sites. Therefore, two evaluation metrics were given a weight of 50% each, meaning that they are considered to be equally important in classifying the producibility of a reservoir. Figure 9 classifies the 273 production scenarios, and the relative highs and lows of the metrics were divided using the medians (85849.71 m^3 and 67 years). The sites with high-yield and low-risk deserve to be classed as I, while the low-yield and high-risk sites are classified as IV. High-efficiency but low-safety sites are classified as II, requiring additional costs in production activities to prevent geo-hazards. High-safety but low-efficiency sites are classified as III, which are unlikely to yield promising results in the short term.

It is feasible to provide several qualitative insights into the effects of geological factors on the producibility classification, which are jointly determined by the economic and safety metrics. To determine the total dimensionless range on producibility of a reservoir, we calculate the weighted average of each factor's independent dimensionless range on economic gain and environmental impact. The order of significance levels of the geological factors influencing the producibility is: $H_1 > \alpha > H_2 > k_1 >$ D $> \rho > S_h > k_2$. For the high economic gain and low environmental impact, the most influential factors are the thickness of hydrate deposits. This implies that this geological factor could

serve as a crucial criterion for rapid screening of optimal sites for production. However, as this study dealt with eight geological conditions and their different combinations in these hydrate accumulations, the interpretation of the classes of the candidate sites remains elusive and needs further research. Moreover, this study reveals only the relative significances of the influential geological factors. The absolute magnitude of the geological parameters is not generalizable due to the subjective limitations of the parameter sampling intervals. The second argument is that it is crucial to note the limitations of the experimental design method of CCD in this study, where it is clear that the number of sampling scenarios is not fully sufficient to support the assured reliability of the conclusions, especially since far too few trials use the extreme combinations of parameter levels.

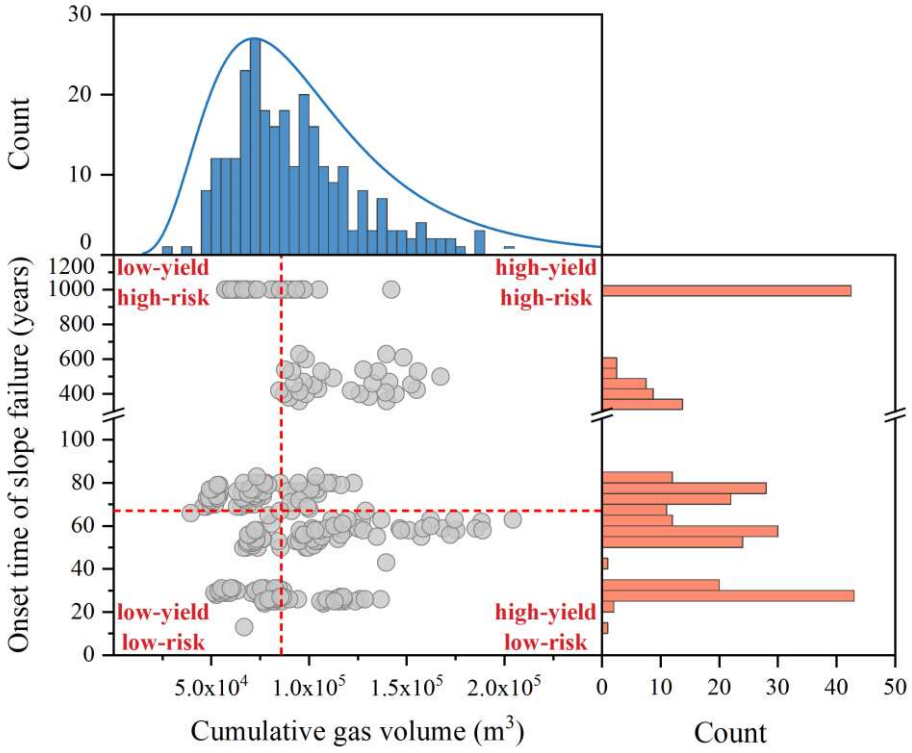

Figure 9. *Multi-objective chosen of hydrate production target*

4 CONCLUSIONS

The economic gain and environmental impact were considered together in the selection of test production target sites, and two evaluation metrics, the cumulative gas volume over 10-year production and the onset time of slope failure under the hypothetical perturbation, were selected to characterize the producibility of a reservoir. The method of central composite design was introduced into the combination of the diverse reservoir geological conditions to generate virtual production sampling scenarios. According to the significance of the factors identified by the range analysis, the factors affecting the cumulative output gas volume are ranked in descending order as follows: thickness of the HBL, permeability of the HBL, burial depth, slope angle, water depth, formation porosity, hydrate saturation, and the permeability of the OL. The factors affecting the landslide onset time are similarly ranked as follows: burial depth, slope angle, thickness of the HBL, hydrate saturation, water depth, formation porosity, permeability of the HBL and the permeability of the OL. In fast screening, optimal sites for extracting gas from oceanic hydrate reservoirs should have thicker hydrate deposits, as it is supposed to show more promise for a high-yield and low environmental impact. The research above illustrates the relative significances of the influential geological conditions in hydrate gas production, and the research results can be effectively used as guidance in the fast screening of optimal sites to advance the commercial exploitation of oceanic methane hydrates.

5 ACKNOWLEDGEMENTS

The work was supported by the National Natural Science Foundation of China (with grants No. U20B6005), and the Fundamental Research Funds for the Central Universities.

REFERENCES

Box, G. E. P., & Wilson, K. B. (1951). On the experimental attainment of optimum conditions. *Journal of the Royal Statistical Society*, 13(1), 1-45.

Chen, L., & Merey, S. (2021). *Emerging technologies in methane hydrate projects*. *Oceanic Methane Hydrates*.

Collett, T. S. (2002). Natural Gas Hydrates. *AAPG Bulletin*, 86(11), 1971-1992.

Goren, A. Y., Recepoğlu, Y. K., & Khataee, A. (2022). *Language of response surface methodology as an experimental strategy for electrochemical wastewater treatment process optimization*. *Artificial Intelligence and Data Science in Environmental Sensing* (Artificial).

Hyodo, M., Nakata, Y., & Yoshimoto, N. (2015). Challenge for methane hydrate production by geotechnical engineering. *Japanese Geotechnical Society Special Publication*, 2(1), 62-75.

Kajiyama, S., Wu, Y., Hyodo, M., Nakata, Y., Nakashima, K., & Yoshimoto, N. (2017). Experimental investigation on the mechanical properties of methane hydrate-bearing sand formed with rounded particles. *Journal of Natural Gas Science and Engineering*, 45, 96-107.

Kong, L., Zhang, Z., Yuan, Q., Liang, Q., Shi, Y., & Lin, J. (2018). Multi-factor sensitivity analysis on the stability of submarine hydrate-bearing slope. *China Geology*, 1(3), 367-373.

Liu, F., Tan, L., Crosta, G., & Huang, Y. (2020). Spatiotemporal destabilization modes of upper continental slopes undergoing hydrate dissociation. *Engineering Geology*, 264(April 2019), 105286.

Lu, L., Zhang, X. H., & Lu, X. B. (2017). Numerical study on the stratum's responses due to natural gas hydrate dissociation. *Ships and Offshore Structures*, 12(6), 775-780.

Moridis, G. J. (2014). *User's Manual for the Hydrate v1.5 Option of TOUGH+ v1.5: A Code for the Simulation of System Behavior in Hydrate-Bearing Geologic Media*.

Nixon, M. F., & Grozic, J. L. H. (2007). Submarine slope failure due to gas hydrate dissociation: A preliminary quantification. *Canadian Geotechnical Journal*, 44(3), 314-325.

Sloan, E. D., & Koh, C. A. (2008). *Clathrate Hydrates of Natural Gases, 3rd ed*. New York: CRC Press.

Song, B., Cheng, Y., Yan, C., Lyu, Y., Wei, J., Ding, J., & Li, Y. (2019). Seafloor subsidence response and submarine slope stability evaluation in response to hydrate dissociation. *Journal of Natural Gas Science and Engineering*, 65, 197-211.

Song, Y., Zhu, Y., Liu, W., Zhao, J., Li, Y., Chen, Y., … Ji, C. (2014). Experimental research on the mechanical properties of methane hydrate-bearing sediments during hydrate dissociation. *Marine and Petroleum Geology*, 51, 70-78.

Sultan, N., Cochonat, P., Foucher, J. P., & Mienert, J. (2004). Effect of gas hydrates melting on seafloor slope instability. *Marine Geology*, 213(1), 379-401.

Tan, L., & Liu, F. (2020). Submarine slope satability during depressurization and thermal stimulation hydrate production with horizontal wells. *Chinese Journal of Theoretical and Applied Mechanics*, 52(2), 567-577.

Tan, L., Liu, F., Huang, Y., Crosta, G., Frattini, P., & Cen, X. (2021). Production-induced instability of a gentle submarine slope: Potential impact of gas hydrate exploitation with the huff-puff method. *Engineering Geology*, 289(May), 106174.

Wang, S., Yan, W., & Song, H. (2006). Mapping the thickness of the gas hydrate stability zone in the South China Sea. *Terrestrial, Atmospheric and Oceanic Sciences*, 17(4), 815-828.

Zander, T., Choi, J. C., Vanneste, M., Berndt, C., Dannowski, A., Carlton, B., & Bialas, J. (2018). Potential impacts of gas hydrate exploitation on slope stability in the Danube deep-sea fan, Black Sea. *Marine and Petroleum Geology*, 92, 1056-1068.